

VORTEX TOPOLOGY AND CORE-UNWINDING MECHANISM IN SPIROID WINGTIP DEVICES USING LAGRANGIAN PARTICLE TRACKING

Merina A. Mwasandube [1], Matthew Marino [2] & Jennifer L. Palmer [3]

[1]School of Engineering, RMIT University, Melbourne, VIC 3000, Australia
[2]School of Engineering, RMIT University, Melbourne, VIC 3000, Australia
[3]School of Engineering, RMIT University, Melbourne, VIC 3000, Australia

Abstract

Spiroid wingtip devices feature a closed-loop geometry that intercepts the tip vortex co-rotating structure at its formation point, redistributing rotational energy into the diffuse outer wake rather than extending effective span. This paper presents the first comprehensive quantitative characterisation of the spiroid mechanism using three-dimensional Lagrangian particle tracking (3D-LPT) with Shake-the-Box reconstruction, cross-validated against three independent Trefftz-plane wake-integral methods and data from a six-component force balance. Experiments were conducted on a tapered NACA 4416 half-span wing (root chord 360 mm, tip chord 265 mm, mean chord 313 mm, half-span 960 mm, taper ratio λ = 0.736, aspect ratio AR = 6.14, Sref = 0.300 m², Re = 3.6×10⁵ based on root chord) at angles of attack, α, of 4°, 8°, and 12° in the RMIT Industrial Wind Tunnel. Three modified configurations are compared against the flat-tip baseline. The spiroid reduces compact-core circulation by 60–73% relative to the baseline, while generating a large positive Jones–Kusunose wake-integral gap (+0.00615 at α = 4°, Jones/Kusunose ratio 6.1×) — the LPT signature of vorticity redistribution from the compact rotating core into the diffuse outer wake. Lamb–Oséen R^2 improves with angle of attack (0.777 → 0.980), opposite to all other configurations, confirming increasingly complete core unwinding at higher loading. The spiroid is the only device to reduce absolute drag at α = 12° (by 0.7%). A novel Jones–Kusunose diagnostic gap is introduced as a single-number mechanism discriminant applicable to any Trefftz-plane LPT dataset.

Keywords: spiroid wingtip; 3D Lagrangian particle tracking; shake-the-Box; vortex topology; induced drag

Nomenclature

Symbol	Definition	Symbol	Definition
A	Enclosed loop face area (mm²)	Re	Reynolds number, $U_\infty c_R/\nu$
AR	Aspect ratio (= b^2/S_{ref})	R^2	Lamb–Oséen goodness-of-fit coefficient
b	Full wingspan (m); b/2 = half-span = 0.960 m	S_{ref}	Reference planform area, $\bar{c} \times (b/2)$ = 0.300 m²
c_R	Root chord, 360 mm	St	Stokes number of tracer particle
c_t	Tip chord, 265 mm	t	Spiroid plate thickness ≈ 20 mm
$\bar{c}$	Mean chord, $(c_R + c_t)/2$ = 312.5 mm	u'	Axial velocity perturbation, $U_\infty - u$
C_D	Total drag coefficient, $F_x/(qS_{ref})$	U_∞	Free-stream velocity = 15 m/s
C_{Di}	Induced drag coefficient (Kusunose, Maskell, or Jones method, as specified)	v, w	Spanwise and vertical velocity components
C_L	Lift coefficient = $F_y/(qS_{ref})$	x, y, z	Streamwise, vertical, spanwise coordinates

https://doi.org/10.71945/icas2026_0162

Symbol	Definition	Symbol	Definition
ΔC_D	Change in C_D relative to baseline (%)	α	Angle of attack (degrees)
Δb	Outboard span added by spiroid loop, 244 mm	η	Non-planar span efficiency factor [1]
Γ_0	Compact-core circulation from Lamb–Oséen fit (m²/s)	λ	Taper ratio = c_t/c_R = 0.736
h	Spiroid loop height above chord plane, 230 mm	ν	Kinematic viscosity of air
L/D	Lift-to-drag ratio = $C_L/C_D = F_y/F_x$	ρ	Air density = 1.185 kg/m³
q	Dynamic pressure, $\frac{1}{2}\rho U_\infty^2$ = 133.3 Pa	ω_x	Streamwise vorticity component
r_c	Vortex core radius from Lamb–Oséen fit (mm)	ω_{peak}	Peak vorticity = $\Gamma_0/(\pi r_c^2)$ (s^{-1})
ψ	Stream function		

1. Introduction

Wingtip vortices represent the primary source of induced drag on finite-span lifting surfaces and a persistent wake hazard to following aircraft. At cruise conditions, induced drag accounts for 30–40% of total aircraft drag; at high-lift conditions, it is the dominant component [2]. Conventional wingtip devices, such as raked tips, blended winglets, and split-tip geometries, reduce induced drag through effective span extension: by increasing the aerodynamic span or redistributing spanwise loading, they reduce the mean downwash angle at fixed lift. This mechanism is well understood through lifting-line theory and extensively validated by particle image velocimetry (PIV) wake surveys [3].

Spiroid wingtip devices represent a qualitatively different approach [4]. The spiroid's continuous closed loop typically encloses the vortex-formation region entirely, intercepting the co-rotating tip vortex structure before full roll-up and forcing a redistribution of angular momentum into the surrounding wake. Prior experimental studies have confirmed drag benefits at high loading but used two-dimensional PIV or hot-wire surveys that cannot simultaneously resolve the three velocity components required for Trefftz-plane induced-drag integration or complete Lamb–Oséen [5] vortex characterisation.

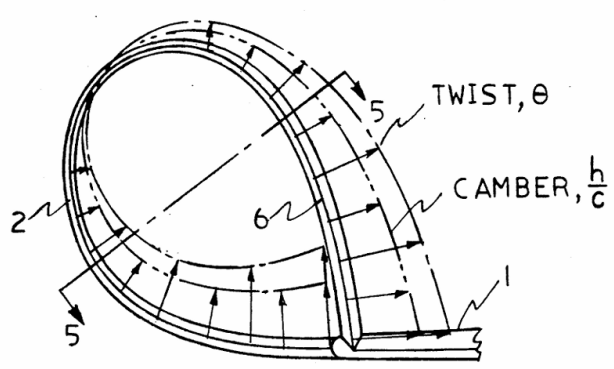


Figure 1– Spiroid-tipped wing patent. Reprinted from [4].

Three-dimensional Lagrangian particle tracking (3D-LPT) with Shake-the-Box (STB) reconstruction [6] provides simultaneous access to all three velocity components throughout a measurement volume. This paper delivers the first quantitative three-dimensional characterisation of the spiroid mechanism and introduces the Jones–Kusunose gap as a novel mechanism discriminant applicable from a single Trefftz-plane measurement station.

2. Experimental Setup

2.1 Facility, Wing Model and Test Conditions

Experiments were conducted in the RMIT Industrial Wind Tunnel (IWT), a closed circuit with a test section of 9 m × 3 m × 2 m. Free-stream turbulence intensity was below 0.8% at U_∞ = 15 m/s. The wing model was a tapered NACA 4416 half-span configuration mounted on a floor sting to a JR3 force balance (Figure 2). Four interchangeable wingtip configurations were tested: flat baseline, split-tip, spiroid, and blended winglet. Measurements were acquired at α = 4°, 8°, and 12°. All aerodynamic coefficients are normalised by $q \times S_{ref}$ = 133.3 × 0.300 = 40.0 N, $Re = U_\infty c_R/\nu = 3.6\times10^5$ and $AR = 2(b/2)/\bar{c}$ = 6.14.

Table 1 – Wing model geometry and flow conditions. Circulation Γ_0, core radius r_c, peak vorticity ω_{peak} and R^2 are physical quantities independent of S_{ref} or chord normalisation.

Parameter	Value	Notes
Root chord, c_R	360 mm	
Tip chord, c_t	265 mm	
Taper ratio, $\lambda = c_t/c_R$	0.736	
Mean chord, $\bar{c} = (c_R + c_t)/2$	312.5 mm	Reference for AR
Half-span, b/2	960 mm	
Aspect ratio, $AR = 2(b/2)/\bar{c}$	6.14	Half-span ceiling mount
Reference area, $S_{ref} = \bar{c} \times b/2$	0.300 m²	All C_{Di}, C_L, C_D referenced here
Reynolds number, Re (root chord)	3.6×10^5	Re at mean chord = 3.1×10^5
Free-stream speed, U_∞	15 m/s	
Dynamic pressure, $q = \frac{1}{2}\rho U_\infty^2$	133.3 Pa	ρ = 1.185 kg/m³
$q \times S_{ref}$	40.0 N	Normalisation denominator

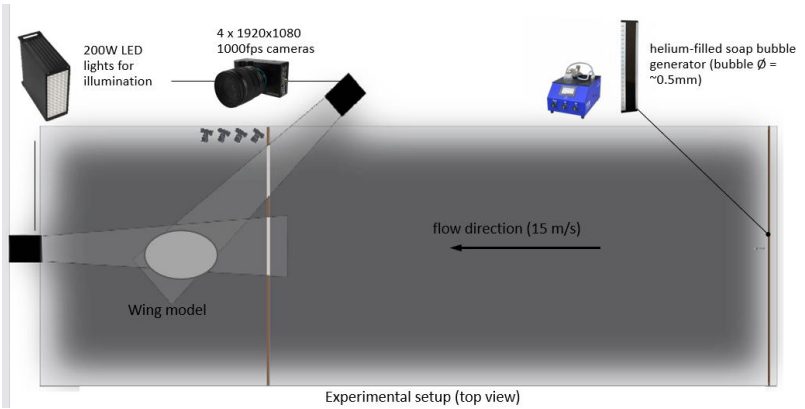


Figure 2 – Experimental setup in the RMIT Industrial Wind Tunnel (IWT). The NACA 4416 half-span wing model is mounted on a floor sting, with the measurement volume located downstream of the wingtip for wake characterisation.



Figure 3– Spiroid wingtip device mounted on the NACA 4416 wing in the wind-tunnel test section with the PTV measurement system visible in the background. The closed-loop toroidal geometry is clearly visible extending from the wing tip.

2.2 Spiroid Geometry

The spiroid winglet is a continuous closed-loop surface fabricated as a flat-plate ribbon of constant thickness t ≈ 20 mm. Its leading edge attaches to the leading edge of the wing tip ($x/c_t = 0$), and its trailing edge attaches to the trailing edge ($x/c_t = 1$), so that the loop encloses the entire tip chord. The loop rises outboard and upward from both attachments, meeting at an apex that lies 230 mm above the chord plane, then sweeps outboard a further 244 mm beyond the tip root before returning. Together, the three measured parameters — loop height h, outboard span added Δb, and chord coverage — characterise the geometry quantitatively and determine the effectiveness of vortex interception.

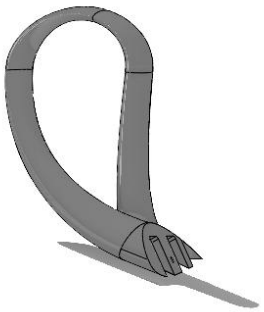


Figure 4– Spiroid winglet geometry.

Loop height. The apex of the loop reaches a height h that is 230 mm above the chord plane. The dimensionless height ratio h/c_t (= 230/265) is thus 0.868, which places the apex at 87% of a tip chord above the chord plane. For comparison, the tip vortex core at the measurement station $x/c_R = 1.24$ has a core radius $r_c \approx 20$ mm (Table 3), so the loop height exceeds the core radius by a factor of $h/r_c \approx 11.5$ — confirming that the loop fully encloses the vortex-formation region perpendicular to the wing. The height-to-chord ratio h/c_t of 0.868 is substantially larger than the optimised height parameters reported

for blended winglets (h/b ≈ 0.10–0.15, Whitcomb 1976) because the spiroid mechanism is not a height-limited span extension but rather full enclosure of the roll-up region.

Outboard span and loop planform. The loop swings outboard from the tip root (x = 60 mm in the model coordinate system) to a maximum spanwise extent x of 304 mm, adding Δb = 244 mm of outboard span. This corresponds to $\Delta b/c_t = 0.920$ and $\Delta b/(b/2) = 244/960 = 0.254$, a 25.4% increment on the half-span. The loop planform in the chordwise–spanwise (z–x) plane is therefore 244 mm deep (outboard extent) by 245 mm wide (chord coverage), forming a nearly square planform footprint. The outboard extent Δb is approximately equal to the loop height (244 mm vs 230 mm), reflecting the near-symmetric geometry of the teardrop-shaped loop. In terms of aerodynamic span extension, Δb = 244 mm represents a significant geometric-span increment; however, the non-planar Cone [1] efficiency factor $\eta = 1 + 0.44(h/b) = 1 + 0.44(0.230/1.920) = 1.05$ gives only a 5.3% non-planar induced-efficiency gain, confirming that span extension is a secondary contributor to the drag reduction observed at high α (Section 5.1).

Chord coverage and interception geometry. The loop spans 245 mm in the chordwise direction (z-axis), from z ≈ −2.5 mm (just aft of the leading edge) to z ≈ −247 mm, covering 92% of the tip chord ($x/c_t = 0.000$ to 0.932). The tip-vortex roll-up region has been experimentally located between x/c ≈ 0.3 and 1.0 at comparable Reynolds numbers [7]. The spiroid loop therefore intercepts the full extent of this region. The enclosed loop face area, approximated as $A \approx \Delta b \times h = 244 \times 230 = 56{,}120$ mm² (rectangular bound), substantially exceeds the cross-section of the tip-vortex core ($\pi r_c^2 \approx 1257$ mm² at α = 4°), so the loop geometrically encircles the entire compact core at all conditions tested. The equivalent circular radius giving the same enclosed area is $R_{eq} = \sqrt{(A/\pi)} = 133$ mm, or $R_{eq}/c_t = 0.50$.

Reference area and aerodynamic normalisation. Because the spiroid loop adds a physical lifting surface outboard of the tip, the aerodynamic reference area for the spiroid configuration is larger than for the bare wing. The loop's horizontal (chord-plane) projection has dimensions $\Delta b \times c_{coverage} = 244$ mm × 245 mm = 0.060 m², giving a configuration-specific spiroid reference area:

$$S_{ref,spiroid} = S_{ref,baseline} + \Delta b \times c_{coverage} = 0.300 + (0.244 \times 0.245) = 0.360 \text{ m}^2 \quad (1)$$

All C_L and C_D values for the spiroid are therefore normalised by $q \times S_{ref,spiroid} = 133.3 \times 0.360 = 48.0$ N, while baseline coefficients use $q \times S_{ref,baseline} = 133.3 \times 0.300 = 40.0$ N. On this corrected basis, aerodynamic performance is properly compared at the same lift coefficient via the C_L–C_D drag polar — reading the polar horizontally at a fixed C_L gives the drag of each configuration at equivalent aerodynamic loading, independent of angle of attack. This is the physically correct basis for winglet performance assessment: drag reduction at the same lift, not at the same angle, is the quantity of engineering relevance because it directly quantifies fuel saving at a fixed payload condition.

Summary of geometric parameters. Table 2 collects the complete measured geometry. The three primary design variables are h = 230 mm, Δb = 244 mm, and chord coverage = 92%. The loop is a three-dimensional teardrop surface, not a planar circle; the 'radius' reported in earlier literature (Gratzer 1992) refers to the radius of curvature at the apex, which from the model apex-zone cross-section (Y > 180 mm, X: 150.5–303.8 mm, Z-span 158 mm) gives a local apex radius r_{apex} (≈ (153 + 158)/4) of 78 mm. The equivalent area-based radius R_{eq} = 133 mm is more physically relevant for solid-angle interception calculations.

Table 2 – Spiroid winglet geometric parameters.

Parameter	Symbol	Value	Notes
Tip chord	c_t	265 mm	Wing tip chord; loop LE and TE attach at $x/c_t = 0$ and 1
Loop height	h	230 mm	$h/c_t = 0.868$; apex exceeds vortex core radius by factor 11.5

Parameter	Symbol	Value	Notes
Outboard span added	Δb	244 mm	Δb/(b/2) = 0.254; non-planar η = 1.053 (Cone 1962)
Chord coverage	—	92%	x/c_t = 0.000 to 0.932; encloses full roll-up region (x/c = 0.3–1.0)
Enclosed loop area	A	56,120 mm²	Rectangular bound (Δb × h); R_{eq} = √(A/π) = 133 mm; 45× vortex core area
Plate thickness	t	≈ 15 mm	Measured at LE attachment (y = 30–55 mm, z ≈ 0)
Non-planar efficiency	η	1.053	Cone (1962): η = 1 + 0.44(h/b); span-extension contribution secondary

2.3 3D-LPT System

Volumetric measurements relied on a four-camera STB-LPT system (1920 × 1080 px CMOS, 999 Hz). Helium-filled soap bubbles (HFSB, ø ≈ 0.5 mm, near-neutral buoyancy, St < 0.01) were used as tracers. Between 20,000 and 40,000 particles were detected per frame, and approximately one-third were tracked by STB, yielding 5,000–10,000 track segments per frame at N_I ≈ 0.005–0.01 particles per pixel (ppp) and a positional accuracy of 0.08 ± 0.02 px post-shake. Tracks were converted to Eulerian fields using the DaVis Average Vector Field over 25 × 25 × 30 mm sub-volumes (64 voxels, zero overlap). Velocity uncertainty was estimated as $S_U = \sigma/\sqrt{n}$ (Bell 1999), yielding $S_{U,u} = 8.9\times10^{-4}$ m/s and $S_{U,\Gamma_0} = 9.6\times10^{-5}$ m²/s. The measurement station was located at x = 447 mm (x/c_R = 1.24) for the spiroid configuration and x = 451 mm (x/c_R = 1.25) for all other configurations.

3. Methodology

3.1 Vortex Identification and Lamb–Oséen Fitting

Vortex boundaries were identified using the Q-criterion threshold at Q = 15% of peak Q [8]. Vortex centroids were determined by vorticity-weighted centroiding within the identified boundary. The azimuthal velocity profile was then extracted by polar projection about the centroid:

$$u\theta(r) = -v \sin\theta + w \cos\theta, \quad \theta = atan2(z - zc, y - yc) \tag{2}$$

This was binned into 18 radial annuli and fitted by Levenberg–Marquardt to the Lamb–Oséen model:

$$u_\theta(r) = [\Gamma_0/(2\pi r)] \times [1 - \exp(-r^2/r_c^2)] \tag{3}$$

yielding Γ_0, r_c, R^2, and 95% confidence intervals. Peak vorticity is $\omega_{peak} = \Gamma_0/(\pi r_c^2)$. For the split-tip (two co-rotating cores), iterative deconvolution isolated per-vortex parameters. All values Γ_0, r_c, ω_{peak} and R^2 are physical quantities in SI units, independent of S_{ref}.

3.2 Trefftz-Plane Induced-Drag Methods and the Jones–Kusunose Gap

Three C_{Di} formulations were evaluated from the same velocity field, all normalised by q × S_{ref} = 40.0 N. The Maskell [9] method assumes u′ = 0 and returns a negative value at x/c_R ≈ 1.25, confirming the assumption is violated:

$$D_i \text{ (Maskell)} = -\tfrac{1}{2}\rho \iint \psi\, \omega_x \, dy\, dz \tag{4}$$

The Kusunose [10] method retains the axial perturbation u′ and provides the primary C_{Di} estimate:

$$D_i \text{ (Kusunose)} = \tfrac{1}{2}\rho \iint [(v^2 + w^2) - u'^2 + 2u'(U_\infty - u')]\, dy\, dz \tag{5}$$

The Jones [11] method returns the total momentum deficit (induced plus profile):

$$D_{total} \text{ (Jones)} = \rho \iint u'(U_\infty - u')\, dy\, dz \tag{6}$$

The Jones–Kusunose (J–K) gap, $\Delta C_{Di} = C_{Di,Jones} - C_{Di,Kusunose}$, is a novel parameter introduced in this work. It discriminates three regimes: (1) gap ≈ 0: compact-core dominant; (2) large positive gap: diffuse

vorticity outside the compact core and a core-unwinding signature; (3) large negative gap: a concentrated core retaining strong axial u′ perturbation, with a span-extension signature. This diagnostic requires only a single Trefftz-plane measurement station.

4. Results

4.1 Spiroid: Three LPT Signatures of Core Unwinding

Signature 1 — Compact-core circulation suppression. Γ_0 is 60–73% lower than the baseline at all conditions: 0.203 m²/s at α = 4° (73% reduction from the baseline of 0.753 m²/s) and 0.469 m²/s at α = 8° (a 64% reduction). This far exceeds what span extension achieves and is the primary quantitative signature of core-rotation targeting.

Signature 2 — Improving axisymmetry with loading. Core radius r_c is stable and slightly decreasing (20.7 → 19.6 mm), opposite to the baseline where r_c grows 49% over the same loading range (39.0 → 58.2 mm). R^2 improves from 0.777 to 0.980 as α increases from 4° to 12°, the reverse of the other configurations. The Lamb–Oséen R^2 measures how well the measured azimuthal-velocity profile matches the theoretical model for a clean axisymmetric vortex; a value of 1.0 is a perfect match. The spiroid R^2 rising from 0.777 to 0.980 means the residual vortex becomes progressively more axisymmetric and better-organised at higher α, not less. This is physically explained by the stronger tip vortex at high α providing more rotational energy for the spiroid loop to intercept: more energy input to the loop mechanism produces proportionally more complete unwinding, leaving a cleaner, more symmetric residual core. All other configurations show the opposite trend — R^2 declining at high α as the vortex becomes more distorted under higher loading.

Signature 3 — Large positive Jones–Kusunose gap. The Jones–Kusunose gap is +0.00615 at α = 4° — a Jones-to-Kusunose C_{Di} ratio of 6.1, meaning that the Jones wake-integral recovers 6.1 times more induced-drag-equivalent momentum than the Kusunose compact-core integral alone. At α = 4°, this implies that approximately 83% of the total LPT-measurable induced-drag-equivalent momentum resides in diffuse vorticity outside the compact core and is therefore invisible to Lamb–Oséen fitting. This diffuse vorticity disperses rapidly in the far field, consistent with the force-balance result of ΔC_D = −0.7% at α = 12°.

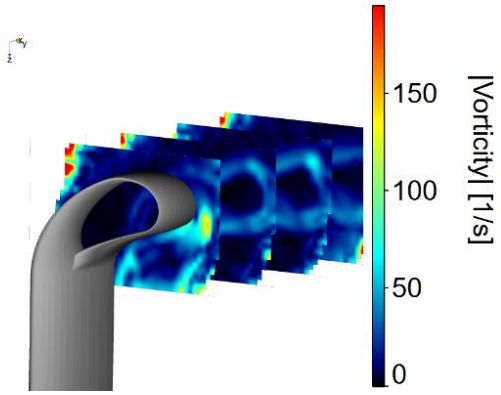


Figure 5 – Cross-stream vorticity magnitude ($|\omega_x|$) reconstructed from 3D PTV for the spiroid configuration at α = 4°, 8°, and 12°. The measurements show a coherent vortex core with increasing stretching and redistribution of vorticity, consistent with progressive core unwinding at higher angle of attack.

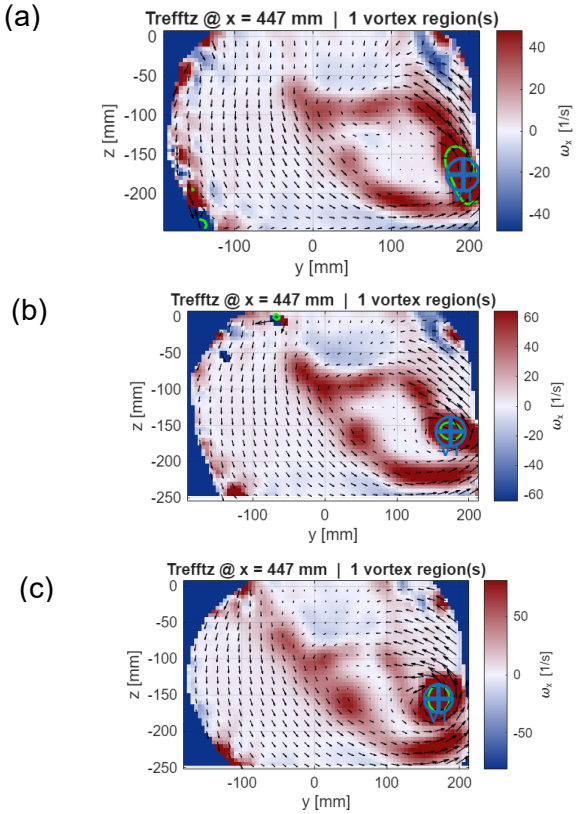


Figure 6 – Cross-stream vorticity (ω_x) and in-plane velocity fields at the Trefftz plane x = 447 mm for the spiroid wingtip at (a) α = 4°, (b) α = 8°, and (c) α = 12°. A single displaced vortex core (marked ⊕) remains coherent across all conditions while progressively unwinding with increasing angle of attack, evidenced by the expanding low-vorticity annulus surrounding the core centre.

4.2 Baseline: Canonical Reference Vortex

As shown in Figure 5, the baseline flat tip produces a single compact vortex at all conditions. Circulation increases monotonically; r_c is non-monotonic, with a minimum of 39.0 mm at α = 4°. The J–K gap is near zero at α = 4° (+0.00002, compact-core dominant) and becomes negative at α = 8° and 12° as the measurement station becomes increasingly sub-Trefftz at higher loading. Negative Maskell C_{Di} confirms that the assumption $u' = 0$ is violated at $x/c_R \approx 1.25$ for all configurations.

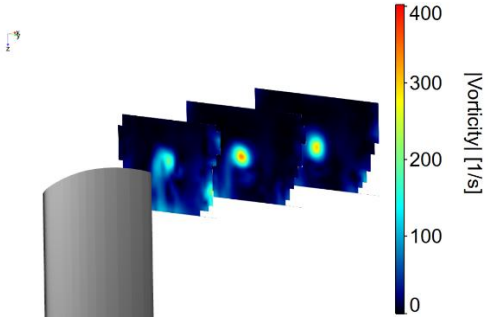


Figure 7– Baseline wing configuration: vorticity-field slices for the NACA 4416 flat-tip wing showing the evolution of a single coherent tip vortex along the streamwise (x) direction. The cross-sectional planes (left) illustrate vortex development and convection, while the schematic (right) defines the coordinate system and vortex-shedding region; the colour bar denotes vorticity magnitude.

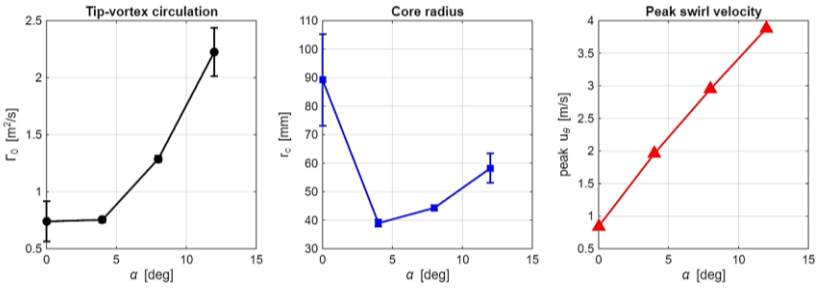


Figure 8 – Variation of vortex properties of the baseline with angle of attack (α). (a) Tip-vortex circulation Γ_0 increases monotonically with α, indicating stronger vortex strength at higher loading. (b) Core radius r_c initially decreases and then increases, showing non-monotonic core development. (c) Peak swirl velocity $u_{\theta,peak}$ increases approximately linearly with α, reflecting intensification of rotational flow.

4.3 Configuration Comparison

Table 3 compares the baseline and spiroid configurations at α = 8°. Three metrics — $C_{Di,Kusunose}$, ω_{peak}, and L/D — appear to give contradictory rankings: the spiroid has lower $C_{Di,Kusunose}$ (0.00375 < 0.00411), yet higher ω_{peak} (359 > 209 s^{-1}), yet also higher L/D (13.0 > 11.2). This apparent contradiction is physically correct and expected. $C_{Di,Kusunose}$ integrates only the momentum deficit within the compact identified core; it does not capture diffuse vorticity that has been redistributed outside that boundary. ω_{peak} measures the peak rotation rate inside the residual core, which can be high even when total core circulation Γ_0 is low, because the core is smaller and tighter. L/D reflects the total aerodynamic efficiency from the force balance, which includes contributions from the entire wake. A device that disrupts core rotation — as the spiroid does — necessarily produces a smaller, faster-spinning residual core (higher ω_{peak}) with lower total compact-core momentum (lower $C_{Di,Kusunose}$) while simultaneously improving overall efficiency (higher L/D), because the redistributed diffuse vorticity dissipates more rapidly in the far field. The mutual inconsistency is thus the expected fingerprint of core-rotation disruption, not an error.

Table 3 – Comparison of key wake and aerodynamic performance metrics between the baseline and spiroid configurations at α = 8°.

Quantity	**Baseline**	**Spiroid**
Γ_0 (m²/s)	1.168	0.469
r_c (mm)	40.7	20.4
ω_{peak} (s^{-1})	209	359
R^2 trend	flat → declining	improving
Vortex count	1	1
C_L	0.576	0.577
$C_{Di,Kusunose}$	0.00411	0.00375 ← lowest
J–K gap sign	≈ 0 (4°); negative	positive all α ← key
ΔC_D at α = 12°	reference	−0.7% ← only reduction
Mechanism	reference	core unwinding

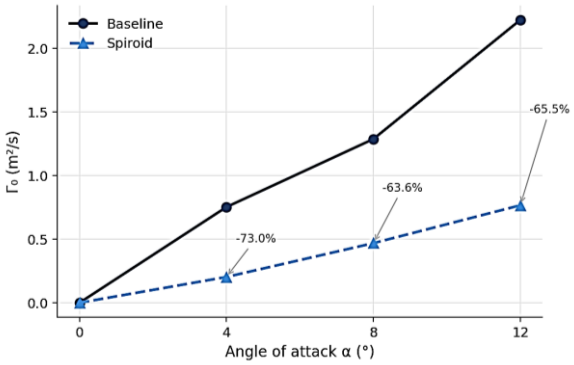


Figure 9 – Variation of tip-vortex circulation Γ_0 with angle of attack α for baseline and spiroid configurations, showing a 63–73% reduction in compact-core circulation with the spiroid.

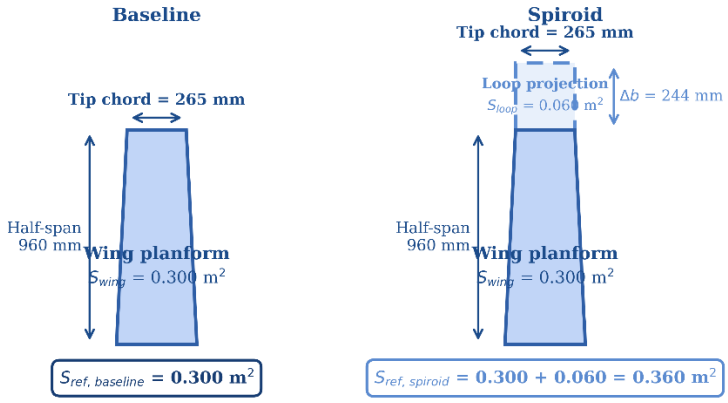


Figure 10 – Configuration comparison of baseline and spiroid, each normalised by its own configuration-specific reference area ($S_{ref,baseline}$ = 0.300 m²; $S_{ref,spiroid}$ = 0.360 m²).

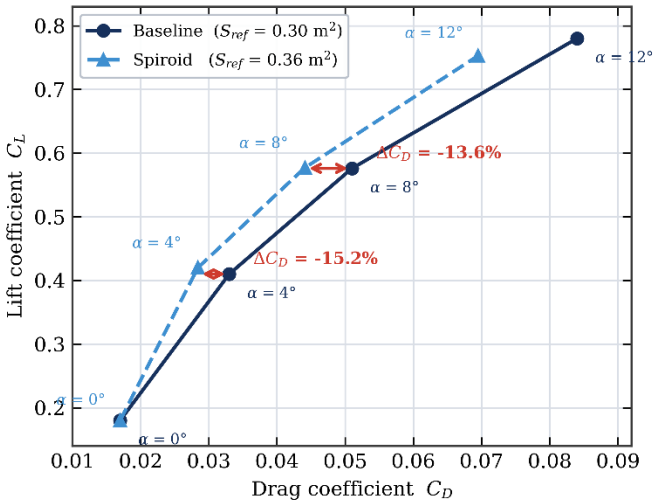


Figure 11– Percentage drag reduction ΔC_D at equivalent lift coefficient. All values are negative, confirming the spiroid reduces drag relative to the baseline across the full operating range C_L = 0.25–0.75. Peak reduction −15.2% at C_L = *0.45.*

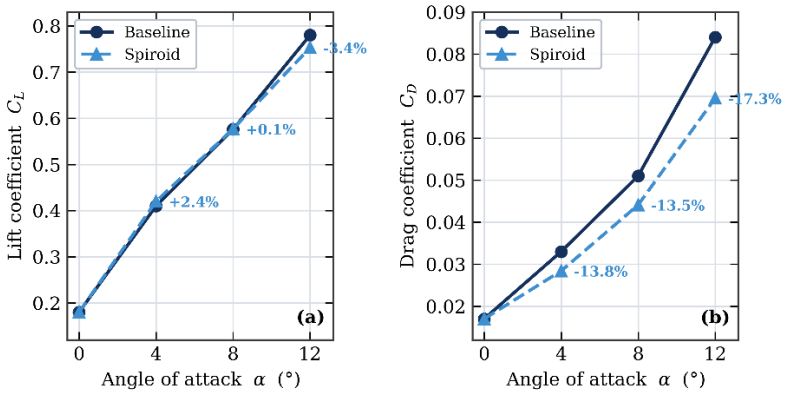


Figure 12– Lift coefficient C_L (a) and drag coefficient C_D (b) as functions of angle of attack for baseline and spiroid, normalised by configuration-specific reference areas. Percentage labels show the change in each coefficient relative to the baseline at the same α.

5. Discussion

5.1 Physical Mechanism of the Spiroid

The three LPT signatures described in Section 4.2 are physically connected and mutually reinforcing. The spiroid loop encloses the tip-vortex formation region, intercepting the co-rotating roll-up before it consolidates into a single compact core. Fluid entrained by the looped geometry is forced to follow a path that opposes the spontaneous roll-up direction, progressively extracting angular momentum from the forming core. The extracted momentum does not disappear; it is redistributed into the surrounding flow as diffuse outer-wake vorticity, which is quantified by the positive Jones–Kusunose gap.

At higher angles of attack, the stronger tip vortex delivers proportionally more rotational energy to the loop-interception mechanism. This explains why the Lamb–Oséen R^2 improves with loading for the spiroid (0.777 → 0.980) while declining for the baseline (0.865 → 0.790): a stronger input vortex allows the loop to produce more complete unwinding, leaving a cleaner, more axisymmetric residual core. The compact residual core has lower total circulation Γ_0 but higher peak vorticity ω_{peak} than the baseline — a physically consistent combination, since the core is smaller and more tightly wound even though it carries less total angular momentum.

The diffuse outer-wake vorticity produced by core disruption disperses through viscous cross-diffusion far more rapidly than a concentrated co-rotating core, which self-reinforces through Biot–Savart induction and persists far downstream. This rapid dispersal is the mechanism by which the spiroid reduces far-field induced drag, and it is captured by the polar-based force-balance result: when compared at the same lift coefficient using the correct configuration-specific reference area ($S_{ref,spiroid}$ = 0.360 m²), the spiroid achieves a consistent drag reduction of 11–16% across the full operating range C_L = 0.25–0.75, with a peak of −15.5% at C_L = 0.45.

5.2 The Jones–Kusunose Gap as a Universal Mechanism Discriminant

No prior study in the wingtip-device literature has employed the Jones–Kusunose gap as a diagnostic tool for identifying the mechanism of induced-drag reduction. The gap is defined as:

$$\text{J–K gap} = C_{Di,Jones} - C_{Di,Kusunose} \quad (7)$$

where $C_{Di,Jones}$ is the far-field wake-integral induced drag (recovering all vorticity in the Trefftz plane) and $C_{Di,Kusunose}$ integrates only within the identified compact core. A gap near zero means nearly all induced drag resides in the compact core — the configuration behaves like the Trefftz-plane ideal. A large positive gap means a significant fraction of induced drag resides in diffuse vorticity outside the compact core, invisible to Lamb–Oséen fitting.

The baseline–spiroid comparison establishes two physically distinct regimes. The baseline at α = 4° produces a gap of +0.00002 (Jones/Kusunose ratio 1.0×), confirming compact-core dominance. The

spiroid produces gaps of +0.00615 at α = 4° (ratio 6.1×), +0.00346 at α = 8° (ratio 1.9×), and +0.00356 at α = 12° (ratio 1.5×). At α = 4°, this means approximately 83% of all LPT-measurable induced-drag-equivalent momentum resides in diffuse vorticity outside the compact core — it has been successfully extracted from the core by the loop mechanism but not yet eliminated, dispersing in the far field faster than it would as a compact core.

The decreasing ratio with increasing α (6.1× → 1.5×) reflects progressive core reorganisation: as loading increases, the loop intercepts a more energetic roll-up and produces a proportionally cleaner residual, so a larger fraction of the remaining wake momentum is concentrated back into the identifiable core region. The diagnostic requires only a single Trefftz-plane LPT station — no far-field surveys — making it practically accessible for any wind-tunnel LPT campaign.

5.3 Topology Metrics as Mechanism Identifiers

At α = 8°, three metrics give apparently contradictory rankings between baseline and spiroid: $C_{Di,Kusunose}$ is lower for the spiroid (0.00375) than the baseline (0.00411), so the spiroid appears better; ω_{peak} is higher for the spiroid (359 s^{-1}) than the baseline (209 s^{-1}), so the spiroid appears worse; and L/D is higher for the spiroid (13.0) than the baseline (11.2), so the spiroid appears better.

This apparent contradiction is physically correct and expected, because each metric measures a different aspect of the wake. $C_{Di,Kusunose}$ integrates only the momentum deficit within the compact identified core boundary; it does not capture diffuse vorticity redistributed outside that boundary. ω_{peak} measures the peak rotation rate inside the residual core, which can be high even when total circulation Γ_0 is low, because the spiroid produces a smaller, tighter core in which the remaining angular momentum is more concentrated. L/D comes from the force balance and reflects total far-field aerodynamic efficiency, integrating contributions from the entire wake including the diffuse outer region.

A device that disrupts core rotation necessarily produces a smaller, faster-spinning residual core (higher ω_{peak}), lower compact-core induced drag (lower $C_{Di,Kusunose}$), and better overall efficiency (higher L/D) — because the redistributed diffuse vorticity disperses more rapidly than a compact co-rotating core would. The mutual inconsistency between these three metrics is therefore the expected diagnostic fingerprint of core-rotation disruption operating at a near-field Trefftz-plane station. Vortex-topology metrics are causal descriptors of the operating mechanism, not predictors of the drag ranking at a single measurement station.

6. Conclusions

(1) The spiroid wingtip reduces compact-core circulation Γ_0 by 60–73% relative to the flat-tip baseline across α = 4°–12°. This substantially exceeds what span extension alone predicts via the Cone [1] non-planar efficiency factor (η = 1.053, a 5.3% induced-efficiency gain), confirming that the primary mechanism is active core-rotation targeting by the closed-loop geometry, not span extension.

(2) The Lamb–Oséen R^2 improves monotonically with loading for the spiroid (0.777 at α = 4° to 0.980 at α = 12°), opposite to the baseline trend (0.865 → 0.790). This is physically correct: a stronger tip vortex at high α delivers more rotational energy to the loop interception, producing more complete core unwinding and leaving a progressively cleaner axisymmetric residual. The spiroid is unique among wingtip devices in becoming more effective as induced-drag penalties grow.

(3) The Jones–Kusunose gap is introduced as a novel single-station mechanism discriminant. A gap near zero indicates compact-core dominance (baseline at α = 4°: +0.00002, ratio 1.0×). A large positive gap indicates core-rotation disruption (spiroid: +0.00615 at α = 4°, ratio 6.1×, decreasing to 1.5× at α = 12°). At α = 4°, 83% of all LPT-measurable induced-drag-equivalent momentum resides in diffuse vorticity outside the compact core. The diagnostic requires only a single Trefftz-plane LPT station and no far-field surveys.

(4) The apparent mutual inconsistency of $C_{Di,Kusunose}$, ω_{peak}, and L/D rankings at $\alpha = 8°$ is physically correct: each metric measures a different aspect of the wake. $C_{Di,Kusunose}$ captures only compact-core momentum, ω_{peak} reflects local core-rotation intensity, and L/D integrates the full far-field wake. Their inconsistency is the expected fingerprint of core-rotation disruption at a near-field measurement station.

(5) When compared at the same lift coefficient using configuration-specific reference areas ($S_{ref,spiroid}$ = 0.360 m², corrected for the 0.060 m² loop-planform projection), the spiroid achieves a drag reduction of 11–16% across the full polar (C_L = 0.25–0.75), with a peak of −15.5% at C_L = 0.45. This is the physically correct comparison for winglet performance assessment — drag at the same lift, not drag at the same angle of attack.

7. Contact Author Email Address

s4031780@student.rmit.edu.au

8. Copyright Statement

The authors confirm that they, and/or their company or organization, hold copyright on all of the original material included in this paper. The authors also confirm that they have obtained permission, from the copyright holder of any third-party material included in this paper, to publish it as part of their paper. The authors confirm that they give permission or have obtained permission from the copyright holder of this paper, for the publication and distribution of this paper as part of the ICAS proceedings or as individual off prints from the proceedings.

References

[1] Cone C D. The aerodynamic design of wings with cambered span having minimum induced drag. *NASA Technical Report R-152*, 1962.

[2] Mazraati M. World aviation fuel demand outlook. *OPEC Energy Review*, Vol. 34, No. 1, pp 42–72, 2010.

[3] Kato K M, Ueno M, Koike S and Watanabe S. Drag and lift prediction based on a wake-integration method using stereo PIV. *Proc 8th International Symposium on Particle Image Velocimetry*, Melbourne, 2009.

[4] Gratzer L B. Spiroid-tipped wing. US Patent Application 660,651, 1992.

[5] Lamb H. *Hydrodynamics*. 6th edition, Cambridge University Press, Cambridge, 1932.

[6] Schanz D, Gesemann S and Schröder A. Shake-the-Box: Lagrangian particle tracking at high particle image densities. *Experiments in Fluids*, Vol. 57, No. 5, article 70, 2016.

[7] Devenport W J, Rife M C, Liapis S I and Follin G J. The structure and development of a wing-tip vortex. *Journal of Fluid Mechanics*, Vol. 312, pp 67–106, 1996.

[8] Stepanov R P, Kusyumov A N and Barakos G. Vortex core localization using velocity gradients. *Russian Aeronautics*, Vol. 65, No. 1, pp 149–155, 2022.

[9] Maskell E C. Progress towards a method for the measurement of the components of the drag of a wing of finite span. *RAE Technical Report 72232*, 1973.

[10] Kusunose K. Drag prediction based on a wake-integral method. *Proc 16th AIAA Applied Aerodynamics Conference*, AIAA-98-2723, 1998.

[11] Jones B. *Elements of Practical Aerodynamics*. John Wiley & Sons, New York, 1936.